UNIVERSITYOF BIRMINGHAM

University of Birmingham Research at Birmingham

Local description of foam flow, deformation and pressure drop in narrow constricted channels

Badve, Mandar; Barigou, Mostafa

Link to publication on Research at Birmingham portal

Local description of foam flow, deformation and pressure drop in narrow constricted channels

Mandar Badve, Mostafa Barigou[*]

School of Chemical Engineering, University of Birmingham, Edgbaston, Birmingham B15 2 TT, United Kingdom

Abstract

We study in extensive detail the flow of dry and wet gas-liquid foams through a narrow two-dimensional channel comprising a complex constriction. The effects of constriction profile and size of aperture, foam flowrate, liquid holdup and liquid viscosity are experimentally investigated and a sophisticated image analysis procedure is developed to extract local fields of foam flow and deformation. Foam dynamics are scrutinised and interpreted in terms of local velocity distribution, elastic strain (texture tensor), plastic deformation (T1 events) and pressure drop. Important foam transformations occur in the vicinity of the constriction. For the first time, the relationship between pressure drop, flowrate and size of constriction aperture is investigated.

Keywords: Foam flow, constriction, elastic deformation, T1 events, pressure drop, friction factor.

[*]Corresponding author - email address: m.barigou@bham.ac.uk

1. Introduction

Applications of gas-liquid foams and solid foams are numerous; they include polymers, food, consumer goods, beauty care, pharmaceuticals, ceramics, foamed concrete, firefighting, oil recovery and mineral particle transport. Recently, new applications have emerged in the medical field, e.g. foam-sclerotherapy for varicose veins, and expanding polymer foam for treating brain aneurysms. Currently the global annual market is approximately $61.9 billion for polyurethane foam (RAM, 2018), $8 billion for shaving foam (Choudhry, 2017), and $74 billion for ice cream (RAM, 2013). Despite these large markets, industrial practice and processes are neither efficient nor optimal because of a severe lack of fundamental understanding of foam science.

Gas-liquid foams are complex structured fluids: they are compressible, non-linear viscoelastic materials; their viscosity is much larger than for the liquid constituent, and they usually exhibit a high zero-shear viscosity which can be mistaken for a yield stress (Barnes, 1999; Jabarkhyl et al., 2020). Understanding of foam properties is therefore limited – design and control for applications is more art than science – and many issues remain unaddressed/unresolved, e.g. flow dynamics, structural behaviour, stability/metastability, and dependence of rheological properties on structure and physicochemical constitution; the recent *Deepwater Horizon* (*BP*) oil spill (Gulf of Mexico, 2010), caused by the failure of a pumped foamed cement, is an example of such a rheological challenge.

Liquid foams are also precursors for solid foams, e.g. food, polymer, concrete, ceramic and metallic; the science of gas-liquid foams is, thus, highly relevant to solid foam structure, both closed- and open-cell. There are two well-described limiting gas-liquid foam structures: (*i*) 'wet' foams have high liquid content and mostly spherical bubbles, e.g. ice cream, with up to ~ 50% continuous phase; (*ii*) 'dry' foams have polyhedral cells and low liquid content, e.g. polyurethane, ~ 5% continuous phase. Bubble size generally ranges from about 10 μm to several mm.

A number of limited empirical studies have been done on bulk foam flow in pipes (Barigou et al., 2003; Deshpande and Barigou, 2000), and recent preliminary experiments and simulations on flow through constrictions have concentrated on idealised two-dimensional foams (Jones et al., 2011). These complex geometries can have significant effects on foam structure and the flow regime, and may destabilise foam structure, giving morphological transformations (Deshpande and Barigou, 2001a, 2001b). For example, the industrial process of foam extrusion, or discharge from a pressure vessel, can change foam texture by (*i*) changes in gas volume fraction and/or bubble growth; (*ii*) flow induced bubble coalescence/aggregation; and (*iii*) changes in liquid phase bulk and surface rheology. These phenomena are not fully understood but are crucial in food processing, e.g. for ice cream flowing through a nozzle. They are also important for flow in or filling of narrow vessels or channels

with complex cross sections. Thus a foam with inadequate rheological properties may not readily flow through narrow passages and constrictions, giving poor 'fill'. Examples include flow of aerated confectionary in narrow channels and complex moulds, filling of cavities with insulation foam, flow of foamed cement slurries in narrow oil-well annuli, filling of hollow aerofoil sections with polyurethane foam to make aerodynamic tethers for communication and geoengineering applications, and production of pre-insulated pipes for district heating.

Because 3D bulk foams are opaque, analysing the properties of a foam passing through complex passages is difficult. Therefore, typically for detailed analysis, experimental and numerical studies have used the flow of single layer of a foam, i.e. a monolayer of bubbles, confined between transparent walls. Such a setup has also been used to study the flow of other complex fluids including emulsions, gels or polymer solutions around obstacles or through constrictions (Langlois, 2014). Foam flow around an obstacle has been studied experimentally by Dollet and co-workers (Dollet et al., 2005; Dollet and Graner, 2007), allowing validation of a so-called 2D viscoelastoplastic model of foam rheology (Cheddadi et al., 2011). Detailed works on foam flow in complex passages are scarce. A few limited experimental/simulation studies have looked at 2D flow of foam through a sudden contraction followed by a sudden expansion where foam experiences both shear and extensional stresses (Dollet, 2010; Jones et al., 2011; Langlois, 2014).

Dollet (2010) in their experimental work (0.2 to 0.4 % liquid holdup) considered a sudden contraction (length = 2, 5, 15 cm; aperture = 1, 2.1, 3.2, 4.4 cm) and concluded that there is an essential coupling between local elasticity, plasticity and flow. Local elastic deformation (elastic strain) is computed using a texture (or elasticity) tensor M, following the definition of Aubouy et al. (2003), whereas local plastic deformation is represented in terms of so-called T1 events (neighbour bubble switching events). Jones et al., (2011) compared experimental results of dry foams (~ 0.5 % liquid holdup) through a sudden contraction (length = 3 cm; aperture = 3 cm) followed by a sudden expansion with predictions obtained from quasi-static simulations conducted using the finite-element Surface Evolver code (Brakke, 1992). Langlois (2014), on the other hand, used Durian's mechanistic Bubble model whereby Newton's equation of motion is solved for each individual bubble, using classical numerical techniques originally developed for Molecular Dynamics, (Durian, 1997) to simulate the flow of wet foam (10 % liquid holdup) through a constriction. Contrary to Surface Evolver, Durian's model treats bubbles as discs not as separate films, accounts for foam dynamic properties, is comparatively simpler to implement and requires less computational time. In conclusion, whereas Langlois' model is suitable for simulating wet/dynamic foams, Jones et al's is applicable to dry/quasi-static foams.

103   This paper reports on an extensive experimental investigation of foam flow behaviour and
104   rheological response in a narrow 2D channel containing a constriction of variable geometry and
105   dimensions including sudden and gradual contraction-expansion types. Foam behaviour is examined
106   as a function of foam flowrate, constriction profile, size of constriction aperture, foam liquid holdup
107   and viscosity of surfactant solution. The local effects on the flow field including foam morphology,
108   topology and velocity distribution are analysed. We examine individual bubble motion and
109   deformation using a texture tensor and record T1 neighbour-switching events, allowing us to obtain
110   the local strain field and hence determine the transition from elastic to plastic response. We also
111   study the local foam pressure drop across the constriction for the various flow conditions considered.
112

113   **2. Materials and methods**

114   **2.1 Experimental setup and procedures**

115   Foam flow experiments were conducted in a custom-made Hele-Shaw cell consisting of two
116   30 mm thick horizontal acrylic plates of 110 cm length and 30 cm width, as depicted in Figure 1a,
117   separated by a uniform adjustable narrow gap so that one or several bubble layers of foam could be
118   accommodated. Prehumidified Nitrogen gas was injected through a 1 mm diameter glass-capillary
119   sparger whilst surfactant solution was injected using an Eldex 3HM piston pump (Cole-Parmer UK).
120   Thus, disordered but nearly monodisperse dry or wet foam with liquid content in the range $1 - 20\%$
121   was generated at the bottom of a vertical acrylic column and allowed to flow into the narrow 2D
122   channel via an inlet pipe, and out of the channel via an outlet pipe downstream where it was collected
123   and the foamate recycled. In all experiments, the area mean bubble diameter (d_{21}) was around 4 mm $\pm$
124   1 mm and remained constant throughout the flow channel, i.e. no bubble coarsening or breakage
125   occurred during the flow.

126   The uniform gap between the two acrylic plates in the Hele-Shaw cell was fixed at 3 mm to
127   accommodate a single bubble layer of foam. To create a flow constriction, two identical constriction
128   plates of thickness 3 mm were inserted and clamped down between the acrylic plates, as depicted in
129   Figure 1b. The spacer plates and constriction plates were all made of black acrylic to minimise the
130   effects of light reflection at edges. The Hele-Shaw cell was divided into two identical parallel flow
131   channels using another 3 mm thick acrylic plate, thus, foam flowing into the gap divides into two
132   identical mirror-image flows, as shown in Figure 1b. Thus, one channel was dedicated to measuring
133   pressure drop at several positions 5 cm apart along the flow (including at the inlet, centre and exit
134   sections of the flow constriction), using a sensitive strain gauge type micro-manometer capable of
135   detecting gauge pressures down to 0.1 mm of water. The pressure tappings were each supplied with a
136   side nitrogen gas bleed through a 0.5 mm capillary to prevent foam from flowing inside the tappings,
137   without affecting the pressure readings, as successfully used in our previous work on foam flow in
138   pipes (Deshpande and Barigou, 2001b, 2001a). The second flow channel, on the other hand, was used
139   solely for visualisation of the foam flow, avoiding the obstruction caused by the pressure tappings.

140   Videos and images of foam flow were recorded using a Basler ace acA1300-200um camera at a rate
141   of 100 to 200 frames per second.

142

143

(a)

(b)

144
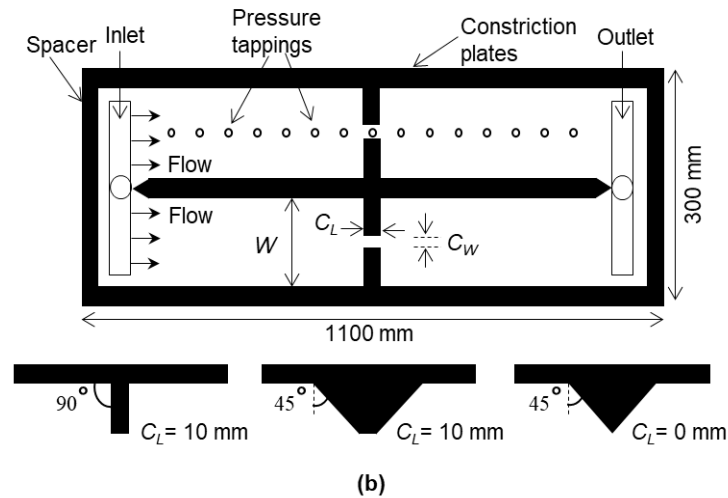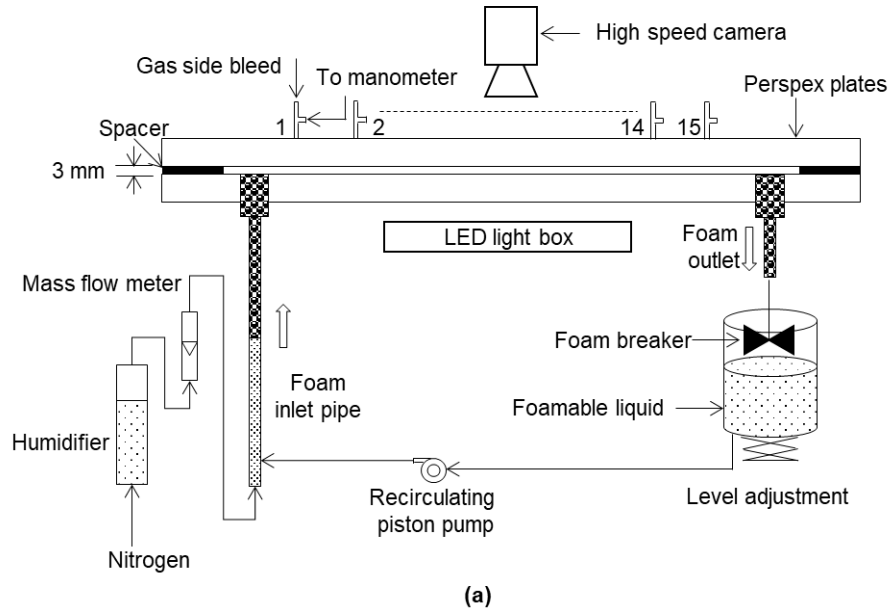
145   Figure 1. Schematic of Hele-Shaw cell foam flow rig: (a) side view; (b) top view and geometric
146   details of the different flow constrictions used.

147

148

149   Three different flow constriction geometries were used: a sudden 90° contraction-expansion
150   and two gradual 45° converging-diverging constrictions having different lengths (C_L = 0 and 10 mm)
151   of the central constricted region (Figure 1b). The width of the flow channel is denoted by W and the
152   width of the constriction (aperture) is denoted by C_W.

153

154   Foam was stabilised using technical grade Sodium Dodecyl Benzene Sulphonate (NaDBS,

155   Sigma Aldrich UK), an anionic surfactant, at a concentration of 2.0 gL^{-1} (equivalent to 5 times its

156   critical micelle concentration) to ensure a consistent surface tension throughout the flow system,

157   dissolved in Type 2 water (equivalent to double distilled water). The surface tension of the NaDBS

158   solution was 32.9 ± 0.1 mNm^{-1} and its viscosity was 1.04 ± 0.03 mPas. The liquid viscosity was

159   varied by dissolving known amounts of glycerol in water.

160

161   Details of the foam flow experiments conducted are summarised in Table 1. Foam dynamics

162   were studied in terms of local velocity distribution, elastic strain (texture tensor), plastic deformation

163   (T1 events) and pressure drop. Sample videos of foam flow experiments are provided for illustration

164   in the Supplementary Information section.

165

Experiment	Angle of converging-diverging section	Size of constriction aperture (C_W), mm	Length of constriction (C_L), mm	Foam flowrate (Q_F), mL.min^{-1}	Foam liquid holdup (ε_L), %	Viscosity of surfactant solution (μ_L), mPa.s
Reference case	90°	10	10	101.01	1	1.04
Effect of foam flowrate	90°	10	10	60.61-202.02	1	1.04
Effect of angle of converging-diverging section	45°, 90°	10	10	101.01	1	1.04
Effect of size of constriction aperture	45°	4, 7, 10, 15	0	101.01	1	1.04
Effect of foam liquid holdup	45°	10	0	101.01	3, 9, 15, 20	1.04
Effect of viscosity of surfactant solution	45°	10	0	101.01	1	1.04, 30.1, 44.7

166   Table 1: Experimental details

167

168   **2.2 Foam flow image analysis**

169   The well-known imageJ software was used for image processing (Eliceiri et al., 2012).   A

170   typical raw image of a foam flowing in the narrow channel is shown in Figure 2a. Figures 2b-c show

171   the steps required to convert the raw image into a network of one-pixel-thick edges (skeletonised

172   image). We first invert the grey levels of the raw image, then threshold them to separate the black

173 network of bubble edges from the white background to make a binary image (black and white; Figure
174 2b). Different zones on the image are treated with different thresholds to compensate for spatial
175 variations in light intensity. In the final step, we "skeletonize" the foam to a network of edges one-
176 pixel-thick (Figure 2c). The same skeletonisation process was used for both dry and wet foams.
177 However, for wet foams, thresholding and binarisation of each image was done using a different
178 imageJ algorithm depending on the liquid holdup, to account for the thick edges of the foam. This
179 process preserves the topology of the foam, ensuring a faithful representation of the real foam which
180 can be used to analyse the dynamics of foam flow in terms of local velocity distribution, texture
181 tensor and T1 events. Another possible approach was to use Voronoi Tesselation to skeletonise the
182 images (Graner et al., 2008) but this yielded the same results. More details on the imageJ software
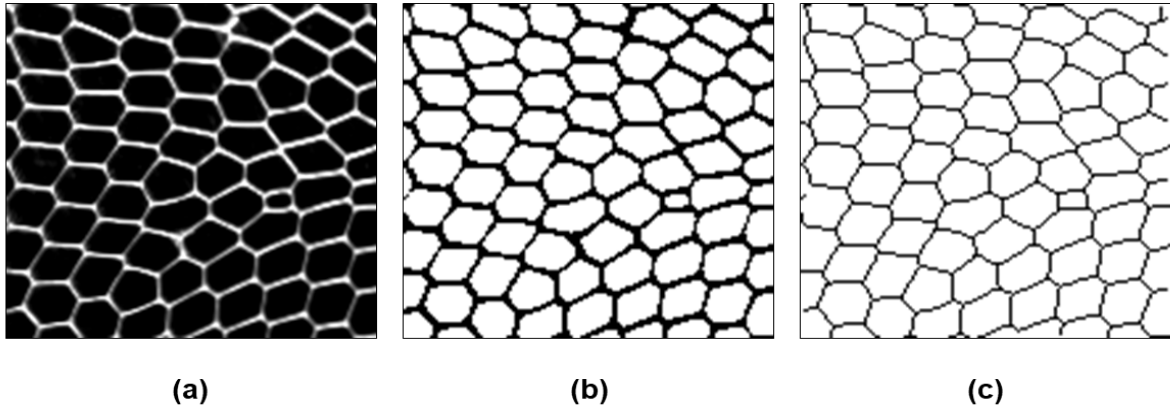183 can be found in the ImageJ User guide (Ferreira and Rasband, 2012).

(a)   **(b)**   **(c)**

184

185 Figure 2. Foam image analysis: (a) raw image; (b) binary image; (c) skeletonized image.
186

187 **2.3 Calculation of relevant foam flow fields**

188 *2.3.1 Local velocity distribution*

189 To measure the local velocity distribution of a foam flowing through a narrow channel with a
190 constriction, we utilised a standard cross-correlation algorithm that is used in the imaging technique of
191 Particle Image Velocimetry (PIV). A white LED light box of dimensions 30 cm × 20 cm was placed
192 below the flow channel to illuminate the foam. In PIV, microscopic tracer particles are used to track
193 the motion of a fluid. In foam flow, tracer particles are not needed since the bubble interfaces in the
194 moving foam themselves scatter light. PIVlab (Thielicke and Stamhuis, 2014), a time-resolved digital
195 Particle Image Velocimetry toolbox available in MATLAB, was used to analyse the skeletonized
196 images. Initial tests revealed that the optimum number of images to be analysed in each experiment
197 was 4000 to avoid statistical bias, and beyond which the mean local velocity distribution was
198 unaffected by the number of images analysed. Multi-pass interrogation windows (four in this case) of
199 size ranging from 50×50 pixels to 20×20 pixels were used in the cross-correlation algorithm. The
200 smallest interrogation window size was slightly larger than the average individual bubble area.

201

2.3.2 Texture tensor

202

203   To analyse the local foam cell deformation, we compute following the definition of Graner et
204 al. (2008) a texture (or elasticity) tensor M which provides an operational definition of deformation
205 which can be experimentally measured and given in terms of averages of microscopic quantities. This
206 was an improvement on previous work by Aubouy et al. (2003) who had used bubble edges rather
207 than the link between neighbouring bubbles, as detecting bubble centres is more accurate. The
208 magnitude of the texture tensor measures the elastic strain of the pattern formed by the bubbles.
209 Considering the link between two neighbouring bubbles to be the vector $v = \begin{pmatrix} x \\ y \end{pmatrix}$, the texture tensor is
210 then defined as:

211

212 $$M = \langle v \times v \rangle = \begin{pmatrix} \langle x^2 \rangle & \langle xy \rangle \\ \langle xy \rangle & \langle y^2 \rangle \end{pmatrix}. \tag{1}$$

213

214 To find the links between neighbouring bubbles on imageJ, the positions of the bubble centres are
215 extracted using an in-house image processing algorithm, followed by a Delaunay triangulation of
216 bubble centres (Ferreira and Rasband, 2012). It should be noted that Jones and Cox (2012) used
217 direct links between bubbles in foam simulations and the Delaunay triangulation in analysing
218 experimental data; the results were indistinguishable. Furthermore, to identify the direct links, one
219 needs to check that the bubbles are touching when defining a link (not always the case in a wet foam).
220 The Delaunay triangulation which requires less computational effort, will also put links in whenever
221 bubbles are close, which are important advantages. Once all such links are identified, using a separate
222 in-house C++ algorithm, each image is divided into a number of interrogation boxes and averaging of
223 triangulated network movement (displacement in x and y direction) is done over all links found in a
224 given box during a given time to compute the tensor in each box. Each local tensor is depicted by an
225 ellipse (Figure 3) whose major and minor axes represent, respectively, the foam cell elongation vector
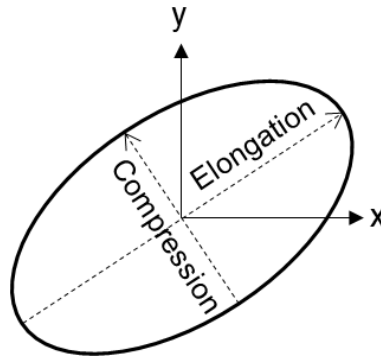226 and compression vector.

227

228   Figure 3. Ellipse representing local texture tensor: major axis represents foam cell elongation vector
229   and minor axis represents its compression vector.

230   To quantify the elastic strain in the foam, we consider the relevant components of the texture

231   tensor M, i.e. the normal components M_{xx} and M_{yy}, to obtain the normal strain difference M_{xx} - M_{yy}.

232   Since the elastic strain scales as a characteristic bubble size, we rescale the normal strain difference by

233   the trace M_{xx} + M_{yy} to compare different bubble areas, as the latter depends on the gas flowrate (Jones

234   et al., 2011). The normal component of the elastic strain or normalised texture tensor component is

235   thus defined as:

236

237   $$M_n = \frac{M_{xx} - M_{yy}}{M_{xx} + M_{yy}}.$$ (2)

238

239   The value of M_n signifies the total extensional strain in the foam and is a more useful parameter for

240   comparing bubble deformation.

241

242   **2.3.3 T1 events**

243   A T1 topological transformation also called T1 event is a neighbour swapping event, i.e. a

244   local plastic rearrangement between bubbles, in which one of the soap films between neighbouring

245   bubbles vanishes and a new film forms. Figure 4 shows a schematic representation of a T1 event:

246   initially, bubbles 2 and 4 are neighbours, but due to external deformation the film separating them

247   (marked in red colour) shrinks in length, resulting in an unstable 4-fold vertex before forming a new

248   film (marked in blue colour). In order to determine the location of T1s we seek four-fold vertices in

249   the experimental images. We then calculate the frequency of T1s and their distribution across the

250   length and width of the flow channel including the constriction region. The distribution and

251   frequency of T1 events provide a local measure of plasticity for foam flowing through 2D narrow

252   channels, thus, highlighting regions where foam is likely to undergo plastic deformation and

253   elucidating how flow dynamics and flow geometry can affect its plasticity.
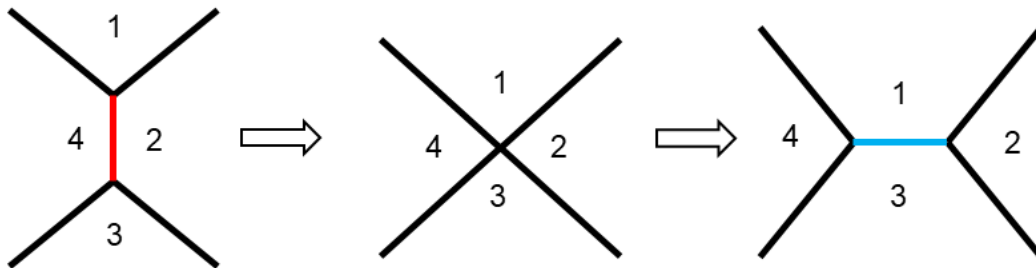
254

255

256   Figure 4. Schematic representation of a T1 event between four neighbouring bubbles: red film
257   disappears and blue film emerges resulting in neighbour bubble switching.

258

3. Results and discussion

We first focus on discussing in detail our reference case experiment: the flow of a nearly monodisperse foam with flowrate 101.01 mLmin^{-1} in the 90° constriction with C_L = 10 mm and ε_L = 1.0%. We then examine the influence of each control parameter listed in Table 1. Results are mainly reported inside an observation window of 10 cm either side of the constriction where the important foam transformations occur.

3.1 Reference case experiment

3.1.1 Velocity field

The full velocity field corresponding to the reference case experiment described above, is depicted in Figure 5. Even at this low flowrate (foam velocity well upstream of the constriction ~ 3 mm/s), no dead zones are observed anywhere in the flow channel. This is in contrast with the flow of viscoplastic fluids (with an apparent yield stress) where dead zones are a common feature (Jay et al., 2002). This confirms that such foams do not possess a yield stress, which is consistent with rheological measurements of various surfactant and protein stabilised foams reported in the literature (Barnes, 2000; Lim, 2005; Jabarkhyl et al., 2020), and contrary to a number of previous presumptions (see for example, Dollet, 2010; Cheddadi et al., 2011; Langlois, 2014). Similar velocity vector maps were reported in experiments with 2D dry foams (ε_L ~ 0.4%) by Dollet (2010) and with wet foams (ε_L ~ 10%) by Langlois (2014). As the foam approaches the constriction, the local velocity increases because of the reduction in flow area. It reaches its maximum value in the middle of the constriction (narrowest section), decreasing thereafter downstream as the area of flow expands (by virtue of mass continuity), as demonstrated by the velocity profile along the central axis of the flow channel plotted in Figure 6a. The divergence of the velocity field is zero well upstream and downstream of the constriction implying that the foam does not manifest its compressibility in these regions. Immediately before reaching the constriction (x ~ − 1.5 cm), however, the divergence turns negative reaching a minimum (~ − 0.5 s^{-1}) at the inlet, and starts to increase again to become positive just before the exit, reaching a maximum (~ + 0.8 s^{-1}) just after the exit (x ~ 0.75 cm), implying compressible flow in the entire vicinity of the constriction with considerable foam density variations as confirmed from mass continuity. There is a small undershoot in the velocity downstream of the constriction. The observed foam compressibility in the vicinity of the constriction and bubble elasticity (elastic deformation of bubbles in transverse direction) might be the prime factors responsible for such undershoot of velocity along central axis. This undershoot has also been observed in the flow of 2D dry foams experimentally by Dollet (2010) and in simulations by Jones and Cox (2012). This type of velocity profile was characteristic of all the experimental cases studied here.
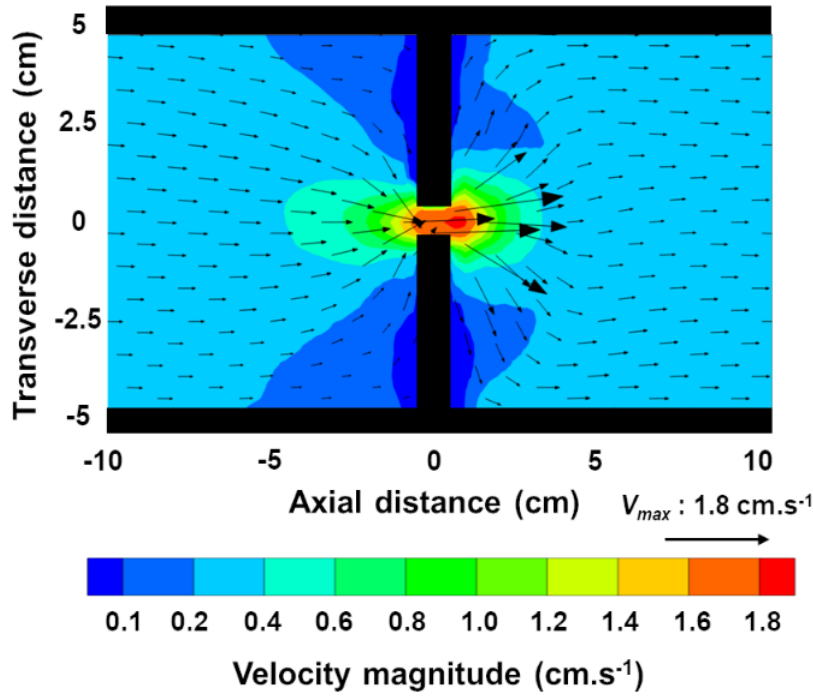
295

Figure 5. Velocity field in foam flowing through a sudden 90° constriction.

Transverse velocity profiles are also plotted across the channel ($y = −4.5$ cm to 4.5 cm), upstream of the constriction in Figure 6b and downstream of it in Figure 6c. There is almost plug flow at the entrance of the observation window ($x = −8$ cm) as there is little variation in velocity across the width of the channel. As the foam approaches the constriciton, the velocity profile is increasingly impacted by the presence of the constriction, becoming very sharp at $x = −1$ cm. The effects of the constriction on the velocity profile are approximately reversed, although there is significant asymmetry in the velocity distribution, as the foam leaves the constriction and moves downstream (Figure 6c); there is first an acceleration at the exit ($x = 1$ cm) leading to a velocity much higher than at the inlet ($x = −1$ cm), followed by a rapid deceleration leading to the velocity undershoot highlighted above and then recovery to mirror the plug flow upstream of the constriction.
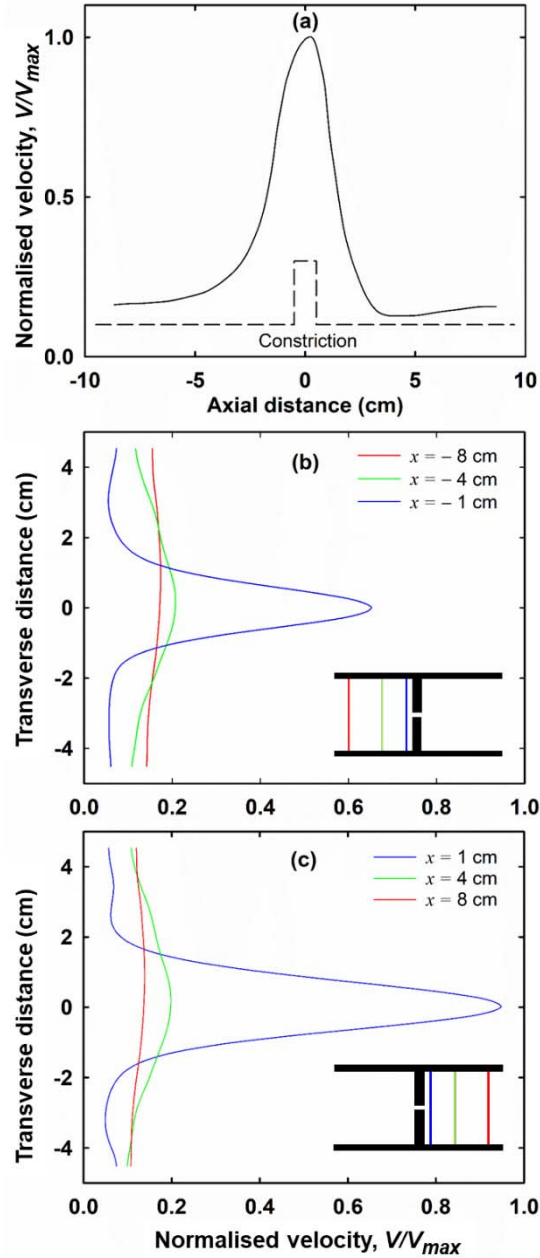
Figure 6. Normalised velocity profiles in sudden 90° constriction: (a) velocity along the central axis of the flow channel; (b) transverse velocity across the width of the flow channel upstream for the constriction; (c) transverse velocity across the width of the flow channel downstream for the constriction.

3.1.2 Elasticity/Texture tensor

To quantify bubble deformation in the reference case experiment, we calculate the texture tensor M defined in Equation (1), and use our ellipse representation (Figure 3) to depict the entire elastic strain field in Figure 7a and plot the normal component M_n in Figure 7b. Bubbles begin to elongate in the spanwise direction at significant distances upstream of the constriction. Comparing the individual components of M_n (data not shown) shows that bubble elongation increases whereas

323   compression decreases, but both increase as the foam approaches the constriction. Such a

324   deformation increases sharply as the foam moves forward reaching a maximum inside the constriction

325   where $M_n \approx 0.52$. Here, bubble elongation and bubble compression (not to be confused with flow

326   compressibility) measured from the individual components of the texture tensor, both increase sharply

327   but elongation dominates by far. Qualitatively similar findings were independently reported by Jones

328   et al. (2011) and by Dollet (2010) for the flow of dry foams ($\varepsilon_L \sim$ 0.2-0.4%) in abrupt constrictions of

329   different length and aperture sizes, including interestingly a similar maximum value of $|M_n|$ (~ 0.5).
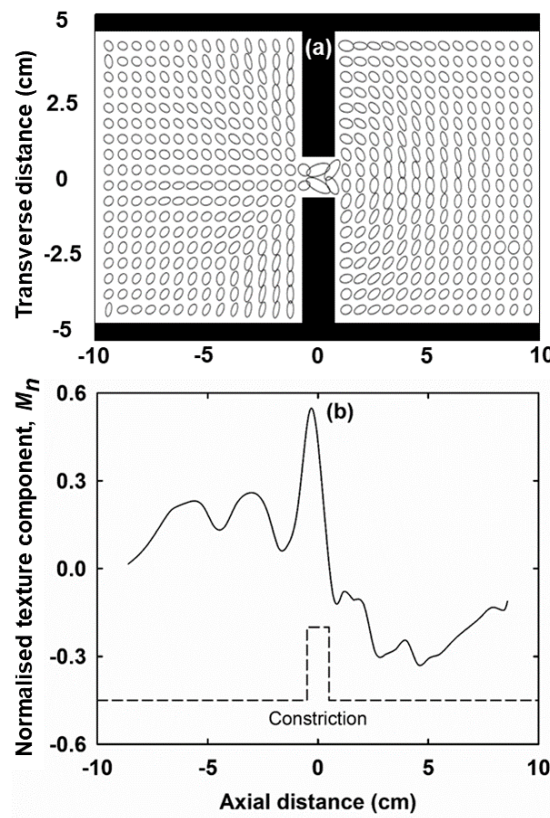
330

331

332   Figure 7. Variations of local texture tensor throughout the flow channel in sudden 90° constriction:
333   (a) ellipse representation of M; (b) axial variations of M_n.

334

335   At the exit section of the constriction, however, both elongation and compression suddenly

336   decrease. There is a brief bubble relaxation followed by an abrupt inversion of the elastic strain in the

337   (negative) transverse direction which continues to increase in magnitude over a distance of a few

338   centimetres. Since bubbles extend spanwise before the constriction, the value of M_n is positive ($M_{xx} >$

339   M_{yy}). Similarly, because the bubbles extend streamwise after the constriction, the value of M_n is

340   negative ($M_{yy} > M_{xx}$). This change in sign occurs exactly at the exit of the constriction, indicating a

341   change in the direction of deformation; elongation increases again and compression decreases, both

342   eventually reaching steady state further downstream. The fluctuations in the average value of M_n,

343   upstream and downstream of the constriction result from the non-uniform flow near the constriction

13

344 and the random rearrangements between bubbles in the form of T1 events. Bubble deformation
345 downstream appears to be slightly lower than upstream. Finally, a gradual elastic relaxation begins
346 tending towards equilibrium, i.e. bubbles tend towards a circular shape beyond a distance of
347 approximately 5 cm with M_n rising towards zero (Figure 7ab). This relaxation phase continues
348 outside the observation window, reaching completion near the exit of the channel.

349

350 *3.1.3 T1 events*

351 Figure 8a shows the local distribution of T1 events over a time interval of 10 s in the
352 reference case experiment, describing the local plastic deformation of the foam. T1 events are
353 concentrated in the vicinity of the constriction where all the significant topological transformations
354 tend to occur, and their number increases with time. Hardly any T1 events were observed far
355 upstream and downstream of the constriction near the edges of the observation window. The
356 distribution of T1 events seems to differ slightly from that reported by Dollet (2010). Such a
357 difference could be due to a variety of factors including the fact that the size (C_W) of the aperture of
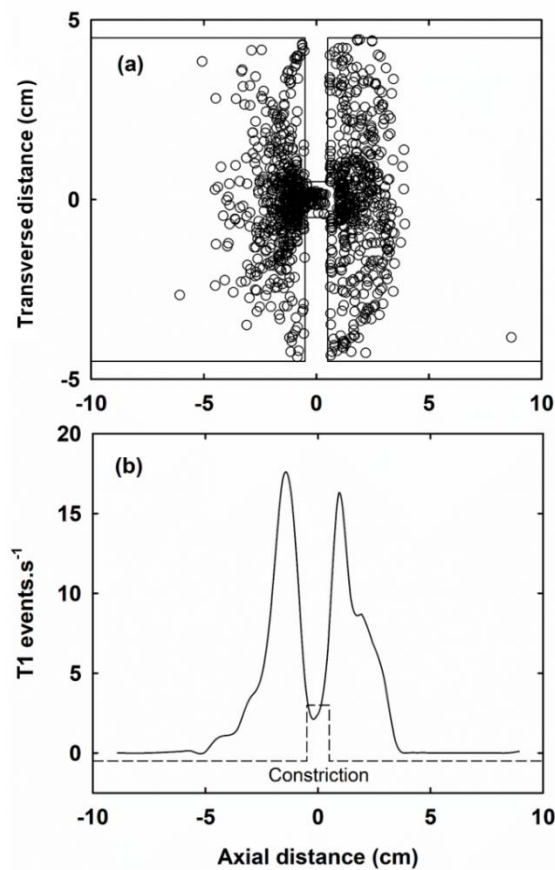358 their constriction was considerably larger than the one used here.

359

360 Figure 8. Distribution of T1 events in sudden 90° constriction during a 10 second time interval: (a)
361 Local distribution of T1 events; (b) Axial variation of total T1events frequency.

362

363   T1 events detected inside narrow vertical bands (4-8 mm wide) across the channel were summed up

364   and a local T1 frequency was obtained by dividing the total by the observation time (10 s), and results

365   are plotted in Figure 8b. Two sharp peaks were observed, just before the constriction and just after,

366   separated by a narrow zone (~ 5 mm) inside the constriction where only a small number of T1 events

367   are detected. As the foam approaches the constriction, bubbles rearrange to squeeze through,

368   resulting in a high occurrence of T1 events and high elastic deformation (see section 3.1.2) confirming

369   the strong link between local plasticity (T1 events) and elastic strain (texture tensor) (Marmottant et

370   al., 2008). Similarly, downstream in the expanding section of the constriction, bubble elongation and

371   rearrangement lead to a high T1 frequency mirroring approximately the behaviour upstream. The T1

372   frequency profile is consistent with results reported by Dollet (2010) and by Langlois (2014).

373

374   **3.2 Effects of control parameters**

375   In this section, we study the influence of the various control parameters (Table 1) and we,

376   therefore, scrutinise the variations of the relevant components of the fields along the length of the

377   channel including the normalised local velocity, normalised component M_n and the frequency of T1

378   events.

379

380   *3.2.1 Effects of foam flowrate*

381   The influence of foam flowrate (60.61-202.02 mL.min^{-1}) was investigated using a 90°

382   constriction with C_L = 10 mm and ε_L = 1.0%. Lower flowrates than these would lead to very small

383   constriction effects on the foam, whilst higher flowrates would lead to the generation of polydisperse

384   foams which are not the focus of this work. Figure 9a shows V/V_{max} along the centreline of the flow

385   channel and the curves almost collapse onto a single master curve, implying that the normalised

386   velocity distribution is independent of flowrate. The velocity undershoot downstream of the

387   constriction, previously observed in the reference case experiment (Figure 6a), reduces with flowrate.

388

389   The variations of M_n along the centreline of the flow channel are depicted in Figure 9b. As

390   the foam flowrate increases, the maximum value of M_n near the constriction also increases gradually

391   by ~ 35% over the whole range, indicating that the bubbles incur more deformation inside the

392   constriction at higher flowrates. However, there is no obvious trend in the variations of M_n upstream

393   and downstream of the constriction.

394

395   Figure 9c shows the frequency of T1 events along the channel for different foam flowrates.

396   There are consistently two major peaks, one peak just before the constriction and one just after. These

397   two peaks are separated by a narrow zone (~ 5 mm) inside the constriction with negligible T1

398   occurrences. The total number of T1 events within the observation window increases approximately

399   linearly as a function of flowrate (Figure 9c); this seems to confirm the earlier prediction by Langlois

400   (2014). An increase in flowrate results in an increase in local strain, which ultimately triggers more

401   T1 events.
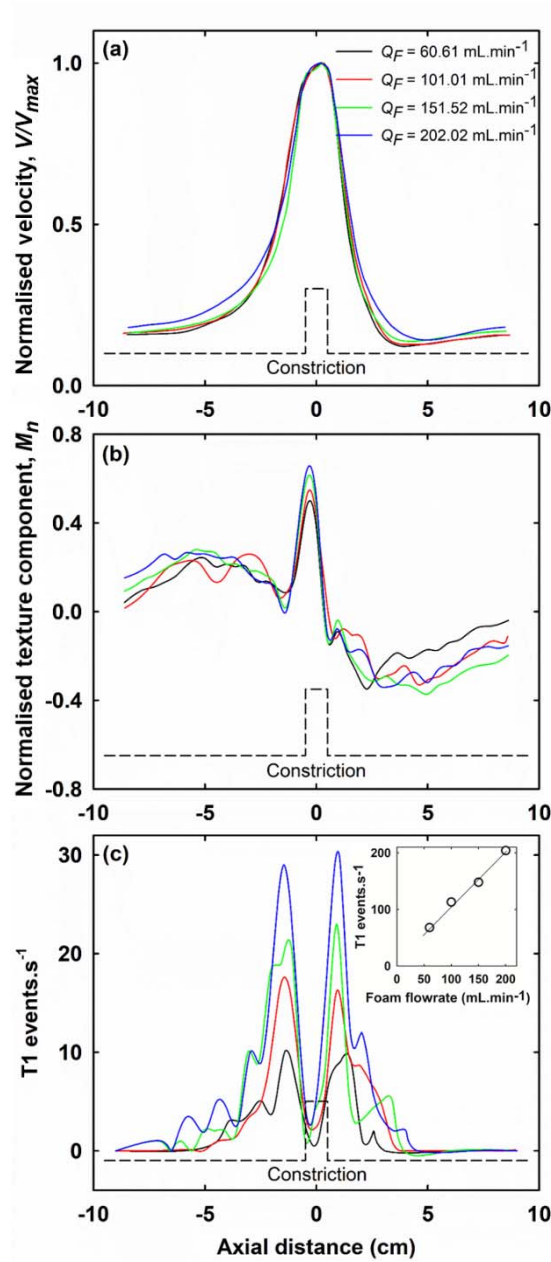
402
403

404   Figure 9. Effects of foam flowrate on: (a) normalised local velocity; (b) normalised texture
405   component; (c) frequency of T1 events.
406

407   *3.2.2 Effects of constriction profile*

408   To study the influence of constriction profile, experiments were conducted using two 45° and

409   90° constrictions both having C_L = 10 mm (Figure. 1b) at a fixed foam flowrate of 101.01 mL.min^{-1}

410   giving ε_L = 1.0%. Features of the flow through the two constrictions are compared in Figure 10.

411   Surprisingly, the velocity curves do not exhibit any major differences. The undershoot observed at

412   the exit in case of the sudden constriction is much less pronounced in case of the gradual constriction.

413   Again, the constriction profile does not have a major impact on the normalised texture component

414   except for the elastic recovery downstream ($M_n \rightarrow 0$) which is much faster for the sudden constriction.

415   There are, however, significant differences in the frequency of T1 events occurring in the vicinity of

416   the constrictions. The peaks just upstream and just downstream of the constriction are much higher

417   for the sudden constriction, and the total number of events is almost double (Figure 10c-e). In the

418   case of the 90° constriction, because of the sudden variation in the area of flow, bubbles experience a

419   higher local strain which results in approximately a doubling of topological changes; however, such

420   rearrangements drop to zero quickly downstream.
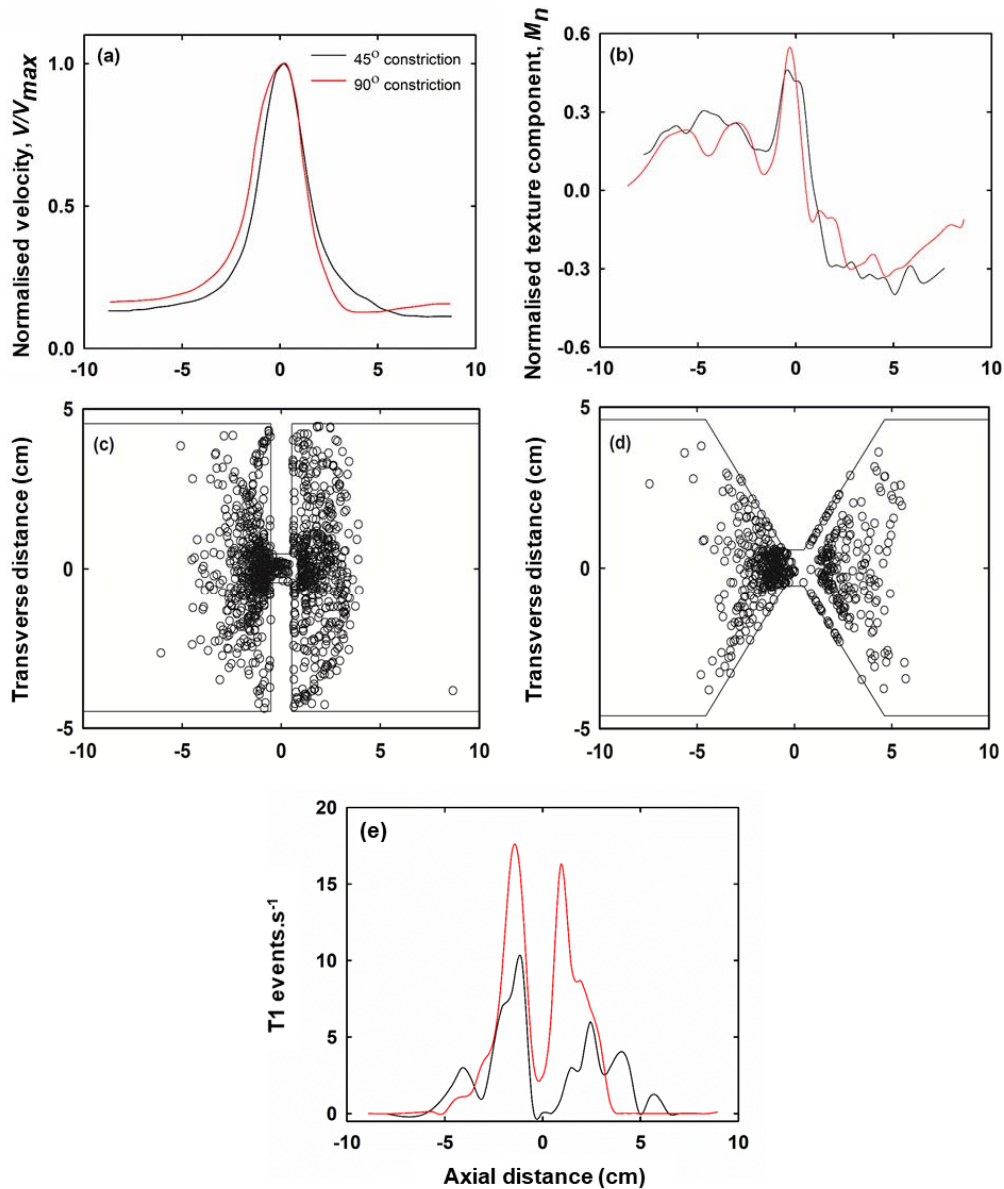

421

422   Figure 10. Effects of constriction profile on: (a) normalised local velocity; (b) normalised texture
423   component; (c) local distribution of T1 events in 90° constriction; (d) local distribution of T1 events
424   in 45° constriction; (e) frequency of T1 events.
425

426 *3.2.3 Effects of size of constriction aperture (C_W)*

427   To study the influence of the size of the constriction aperture (C_W), we image foam with $\varepsilon_L =$

428   1.0% flowing at 101.01 mL.min^{-1} through a 45° constriction with $C_L = 0$ mm (Figure 1b), but varying

429   C_W from 4 to 15 mm, whilst the bubble size was constant with $d_{21} = 4 \pm 1$ mm. The axial velocity

430   profiles shown in Figure 11 collapse approximately on a single curve irrespective of the constriction

431   aperture size.

432

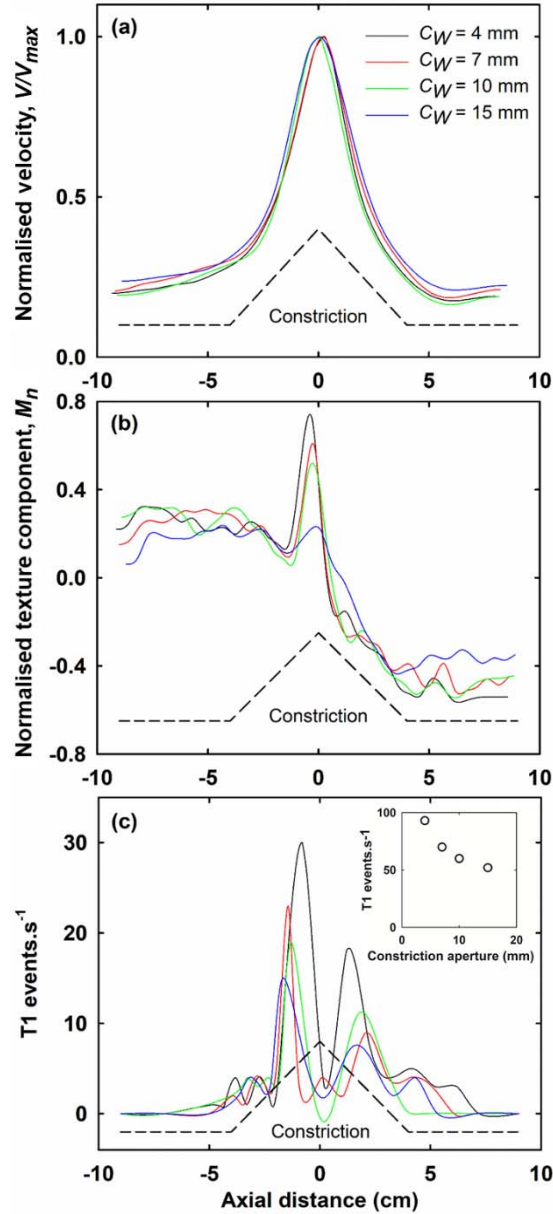433   Figure 11. Effects of size of constriction aperture (C_W) on: (a) normalised local velocity; (b)
434   normalised texture component; (c) frequency of T1 events.

435
436   The main differences between the M_n profiles occur at the centre of the constriction, showing

437   increasing elastic deformation for narrower apertures.   For all constrictions, M_n falls off rapidly to

18

438 zero as the foam leaves the constriction, changes sign and continues to increase in magnitude before

439 reaching a plateau with bubbles emerging from narrower constrictions exhibiting more deformation;

440 eventually M_n is expected to rise to zero near the exit of the channel. The greater the C_W value the

441 smaller the total number of T1 events (Figure 11c). As the size of the constriction aperture increases,

442 the foam undergoes less deformation and hence less T1 events are observed.

443

3.2.4 Effects of foam liquid holdup

445   The effects of the foam liquid holdup (1.0% – 20%) was investigated using a foam flowing at

446 a fixed flowrate of 101.01 mL.min^{-1} through the 45° constriction with $C_L = 0$ mm (Figure 1b). Within

447 the conditions investigated, varying ε_L did not produce any significant effect on the axial velocity

448 profile, as shown in Figure 12a. On the other hand, the transverse velocity profiles depicted in Figure

449 12b, show considerable differences. These velocity profiles become flatter (i.e. tends to plug flow) as

450 ε_L increases. We express the overall uniformity of such profiles using the uniformity index I:

451

452 $$I = \frac{\sum w_i}{n} \tag{3}$$

453

454 where, $w_i = \frac{\sqrt{(V_i - \overline{V})^2}}{\overline{u}}$ is a measure of local uniformity; V_i is the local velocity at location i and $\overline{V}$ is

455 the mean velocity at n locations across the flow channel at $x = -8$ cm. For ideal plug flow, $I = 0$. As

456 ε_L increases from 1.0% to 20%, I reduces from 0.042 to 0.008, approaching zero. Thus, in contrast to

457 dry foams, wetter foams tend to approach the constriction in the plug flow regime. The same

458 behaviour was observed downstream, as the foam moved away from the constriction. With an

459 increase in liquid holdup, the Plateau borders sliding on the wall become thicker, hence, causing less

460 sliding friction which is consistent with pressure drop measurements (section 3.3). In consequence, as

461 shown in Fig. 12c, this reduces elastic deformation in the foam and, hence, velocity variations also

462 reduce, tending towards plug flow. Plug flow was observed in wet foams flowing in pipes

463 (Deshpande and Barigou, 2000).

464

465   The variations of M_n depicted in Figure 12c show that dry foams experience significantly

466 more deformation than wet ones inside the constriction as well as upstream and downstream of it.

467 With more liquid present in foam, the lubricating liquid layer on the wall is thicker, thus, reducing the

468 wall sliding friction, i.e. the wall shear stress and, hence, the elastic strain. Using numerical

469 simulations, and in agreement with experimental findings from the literature, Marmottant *et al*. (2008)

470 concluded that elastic deformation in foams flowing past obstacles decreased with liquid holdup.

471 Cheddadi et.al (2011) who studied flow of foams past obstacles experimentally, also reported more

472 elastic deformation (twice the maximum M_n value) in the case of a dry foam ($\varepsilon_L =1.2$ %) compared to

473   a wetter foam (ε_L =7 %). The frequency of T1 events (Figure 12d), however, does not show a clear

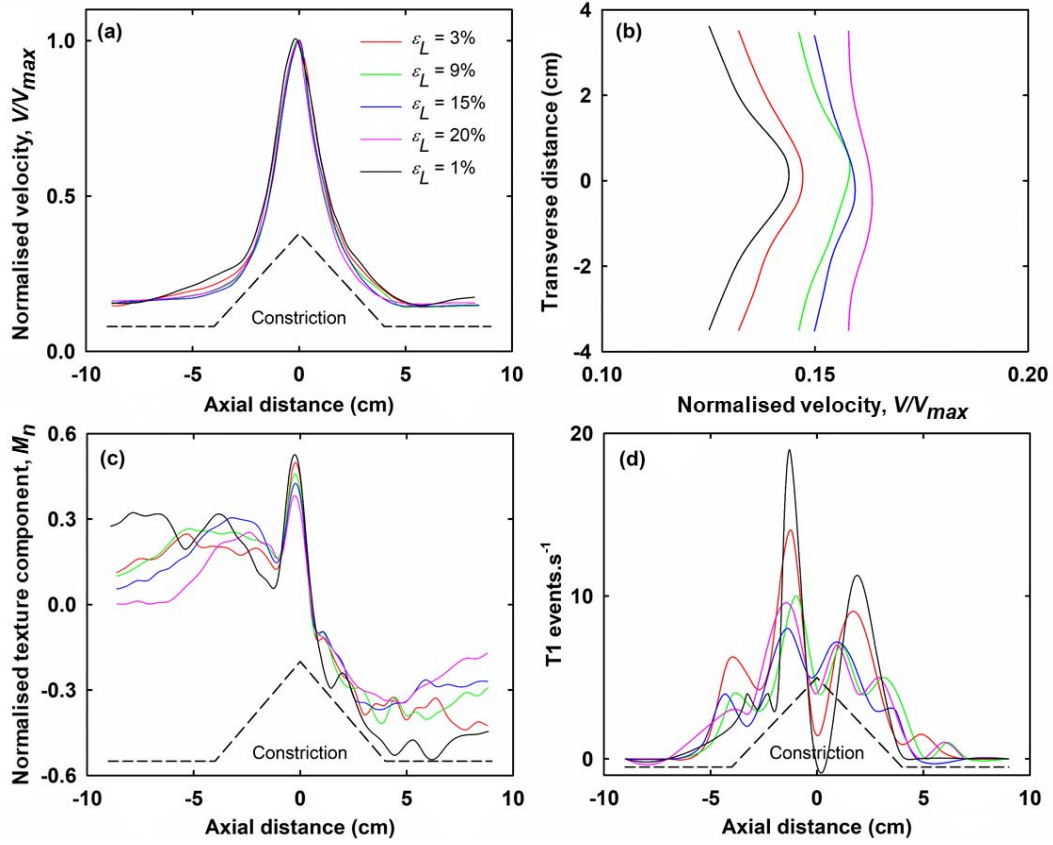474   trend; as ε_L increases, it remains more or less the same.

475

476

477   Figure 12. Effects of foam liquid holdup (ε_L) on: (a) velocity along the central axis of the flow
478   channel; (b) velocity across the width of the flow channel at $x = -8$cm; (c) normalised texture
479   component; (d) frequency of T1 events.

480

481   ### *3.2.5 Effects of viscosity of surfactant solution*

482   The viscosity of the surfactant solution (μ_L) was varied within the range $\mu_L = 1.04 - 44.7$

483   mPa.s, using the 45° constriction with $C_L = 0$ mm (Figure 1b) at a fixed flowrate of 101.01 mL.min^{-1}

484   ($\varepsilon_L = 1.0\%$). Within the conditions investigated, varying μ_L did not produce any significant effect on

485   the axial velocity profile, as shown in Figure 13a. There are no discernible effects on M_n upstream of

486   the constriction (Figure 13b). However, as the foam interacts with the constriction, foams formed

487   from more viscous liquids experience significantly less elastic deformation, positive inside and

488   negative on exit of the constriction; the rate of liquid drainage in the Plateau borders slows down

489   making them and the liquid films slightly thicker, thus, probably enhancing inter-bubble

490   mobility/slippage and reducing deformation (Deshpande and Barigou, 2000). Whilst lower viscosity

491   foams seem to incur more T1 transformations at the inlet of the constriction and less inside, such

492   differences vanish as the foam leaves the constriction (Figure 13c).
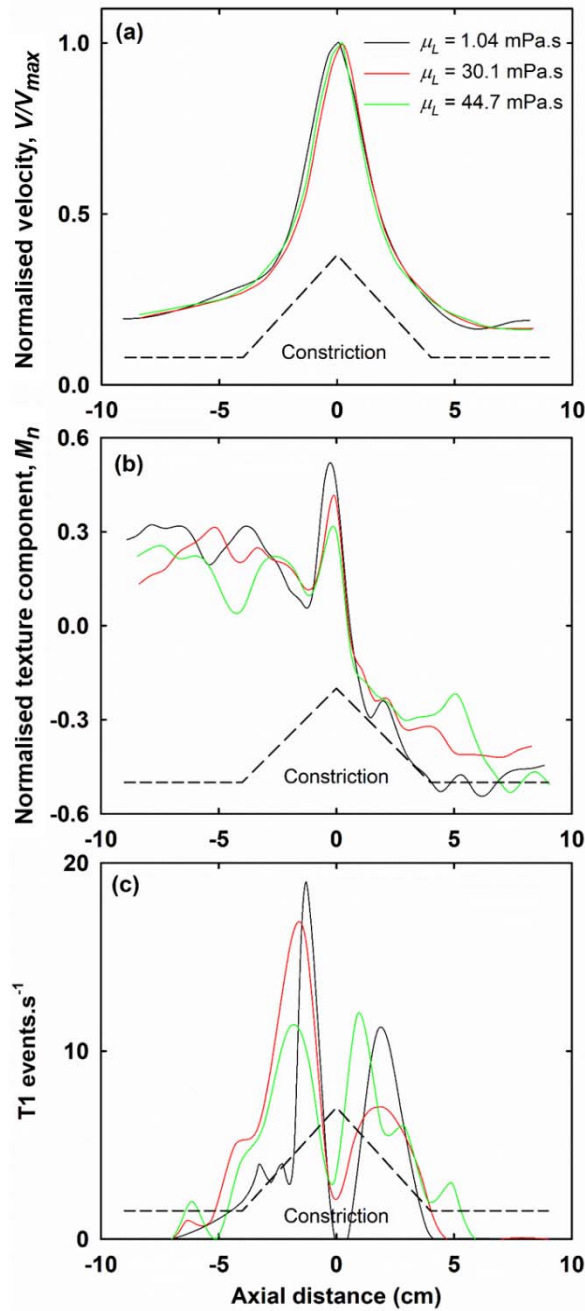
493

494

495   Figure 13. Effects of viscosity of surfactant solution on: (a) normalised local velocity; (b) normalised
496   texture component; (c) frequency of T1 events.

497

3.3 Pressure drop in foam flow

499   Pressure drop was measured along the whole flow channel including the constrictions

500   described in Figure 1b. Typical profiles are shown in Figure 14a for foam with $\varepsilon_L = 1.0\%$, and a 45°

501   constriction ($C_L = 0$ mm, $C_W = 10$ mm). The Piezometric pressure varies approximately linearly along

502 the length of the channel both upstream and downstream of the constriction. There is a slight drop in

503 the slope of the line downstream compared to upstream. The constriction causes a significant local

504 pressure drop. The flow being horizontal, the entire pressure drop is attributed to the sliding friction

505 at the walls of the channel. These results are consistent with earlier observations concerning the flow

506 of bulk foams in pipes (Deshpande and Barigou, 2001b, 2000; Wiggers et al., 2000). The effects of

507 varying the size of the constriction opening are depicted in Figure 14b. As expected, narrower

508 constrictions generate much larger local pressure drops, but the trend is approximately linear as a

509 function of foam flowrate for all constriction sizes. As discussed above (section 3.2.3), reducing the

510 constriction opening leads to more intensive bubble rearrangements (i.e. more elastic strain and more

511 T1 topological transformations) and, hence, more energy dissipation.

512

513   Foam pressure drop in the straight channel and across the constriction also varied as a

514 function of constriction profile, foam liquid holdup and liquid viscosity. Pressure drop results for

515 flow through a sudden 90° constriction showed similar trends as the 45° constriction, but were 1.2 –

516 1.5 times higher (data not shown), depending on flow conditions. Across the constriction, this

517 increased pressure drop may be attributed to the occurrence of more T1 events in a 90° constriction,

518 causing more velocity fluctuations, thus, leading to more friction between bubbles and between

519 bubbles and channel walls. Wetter foams experience less pressure drop, but a higher liquid viscosity

520 leads to a higher pressure drop throughout the channel including the constriction. Such a pressure

521 drop stems from the shear in the lubricating thin liquid film on the channel walls (Deshpande and

522 Barigou, 2000). The wall film thickness cannot be readily measured but an effective thickness, δ, can

523 be calculated from:

524

525 $$\tau_w = \frac{\mu_L V_F}{\delta}$$ (4)

526

527 where τ_w is the wall shear stress and V_F is the mean foam velocity. Values of $\delta = 1 - 10$ μm were

528 reported for foam flow in vertical pipes (Deshpande and Barigou, 2000). Our estimates of δ were in

529 the range 5–40 μm depending on flow conditions. The higher values of δ may be due to the

530 horizontal direction of the flow. A higher liquid holdup increases δ, which for a given surfactant

531 solution viscosity and foam flowrate results in less pressure drop.
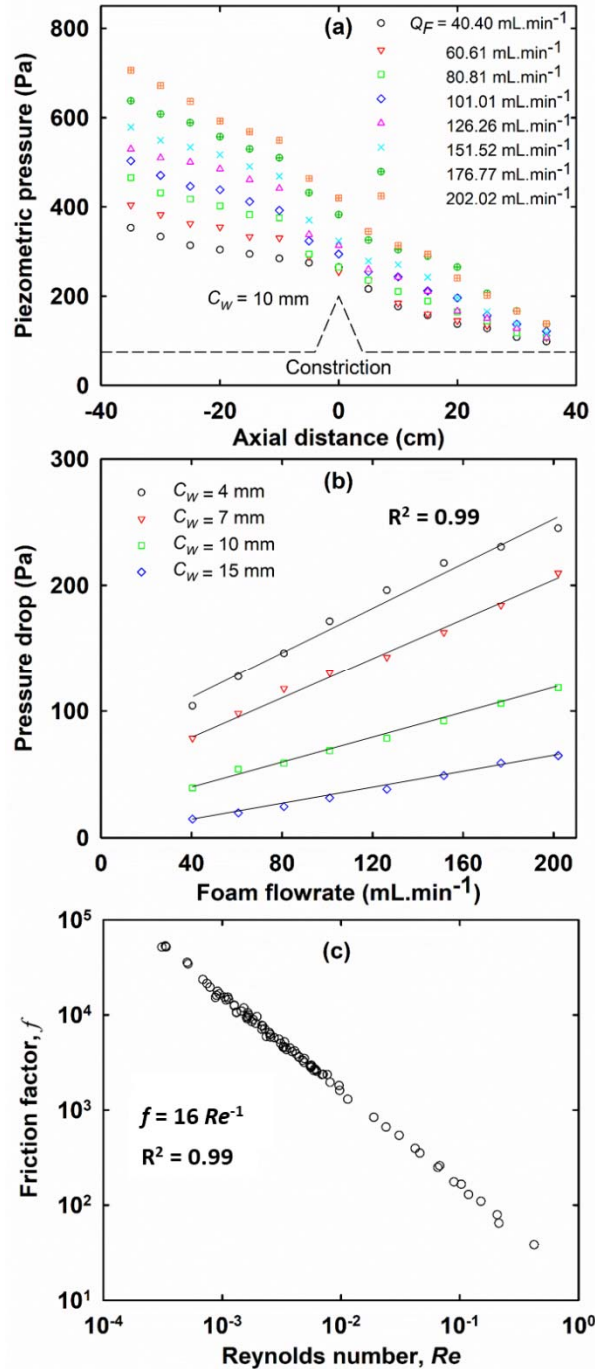
Figure 14. Pressure drop in foam flow with 45° constriction (C_L = 0 mm): (a) Piezometric pressure profile along the channel for different flowrates; (b) pressure drop across the constriction for different constriction apertures; (c) Fanning friction factor for foam flow in straight sections of the channel for different flowrates, constriction apertures, foam liquid holdup and viscosity of surfactant solution.

The straight sections of the flow channel contributed by far the largest part to the total pressure drop. The description of fluid flow by a friction factor is very useful for pressure drop calculations and the design and analysis of flow systems. As the motion of foam under the present conditions is mainly governed by the sliding action on the wall, the similarity between 2D and 3D flow can be reasonably assumed. Therefore, the approach of Deshpande and Barigou (2000), who

543 studied the pressure drop in foam flow through straight vertical pipes, is adopted here. The rheology

544 of the foam flowing in the straight parts of the channel is described by considering the gas-liquid

545 system as non-Newtonian pseudo-homogeneous fluid. Full details of the theoretical derivations can

546 be found in Deshpande and Barigou (2000). It follows from this theory that for a foam obeying exact

547 power-law rheology, the Fanning friction factor is given by $f = 16/Re$ where Re is the generalised

548 Reynolds number given by:

549

550 $$Re = \frac{\rho_F V_F^{2-n} h^n}{2^{n-3} k \left(3+\frac{1}{n}\right)^n}$$ (5)

551

552 where h is the height of the flow channel, V_F is the mean foam velocity in the channel, ρ_F is the foam

553 density determined from the mass flowrate of foam, and k and n are the power-law parameters. The

554 friction factor data plotted in Figure 14c lie remarkably on a unique line and are well fitted by the

555 expression:

556

557 $$f = \frac{16.0}{Re} \qquad (r^2 = 0.99)$$ (6)

558

559 where the power law model parameters obtained from the experimental data lie within the ranges: 0.1

560 $\leq k \leq 0.21$ and $0.4 \leq n \leq 0.75$) Given that the foams studied here consist of a single bubble layer

561 moving in a 2D channel, this shows that the relationship $f = 16/Re$ is universal for foam flow. This

562 result has practical significance in that pressure drop in foam flow through a series of channels of

563 different dimensions can be calculated using a constant friction factor.

564

565 **4. Conclusions**

566 Considering the entire foam flow field, no dead zones exist anywhere in the channel even at

567 the slowest flowrates, confirming the non-existence of a yield stress. Important foam transformations

568 occur in the vicinity of a flow constriction. The wetter the foam, the more it tends to approach the

569 constriction in the plug flow regime. With an increase in foam flowrate and decrease in size of

570 constriction aperture, foam pressure drop, local elastic strain and plasticity increase. More pressure

571 drop and local plastic deformations are manifested across a 90° constriction compared to a 45°

572 constriction, but downstream of the constriction, foam relaxation is faster. A higher liquid holdup and

573 liquid viscosity reduce both local elastic and plastic deformations. There is a strong link between

574 local plasticity (T1 events) and local elastic strain (texture tensor); a high elastic strain translates into

575 a high plastic deformation. Such a transition occurs in the vicinity of the constriction. A higher foam

576 liquid holdup increases the thickness of the lubricating liquid film on the wall, which for a given

577 liquid viscosity and foam flowrate results in less pressure drop. Pressure drop through straight narrow
578 channels can be predicted using a constant friction factor. The relationship established here between
579 pressure drop, flowrate and aperture size is a novel result which is of great importance to industrial
580 applications, and could not be investigated in previous quasi-static foam studies.
581
582 **Acknowledgments**

586
587

References

Aubouy, M., Jiang, Y., Glazier, J.A., Graner, F., 2003. A texture tensor to quantify deformations. Granul. Matter 5, 67–70. https://doi.org/10.1007/s10035-003-0126-x

Barigou, M., Deshpande, N.S., Wiggers, F.N., 2003. Numerical Simulation of the Steady Movement of a Foam Film in a Tube. Chem. Eng. Res. Des. 81, 623–630. https://doi.org/https://doi.org/10.1205/026387603322150471

Barnes, H., 2000. A Handbook of Elementary Rheology. University of Wales, Institute of Non-Newtonian Fluid Mechanics.

Barnes, H.A., 1999. The yield stress—a review or 'παντα ρει'—everything flows? J. Nonnewton. Fluid Mech. 81, 133–178. https://doi.org/10.1016/S0377-0257(98)00094-9

Brakke, K.A., 1992. The Surface Evolver. Exp. Math. 1, 141–165. https://doi.org/10.1080/10586458.1992.10504253

Cheddadi, I., Saramito, P., Dollet, B., Raufaste, C., Graner, F., 2011. Understanding and predicting viscous, elastic, plastic flows. Eur. Phys. J. E 34, 1–15. https://doi.org/10.1140/epje/i2011-11001-4

Choudhry, K., 2017. Lindal's Actuator Targets the Shaving Gel and Foam Market [WWW Document]. URL https://www.beautypackaging.com/issues/2017-10-01/view_design-center/lindals-actuator-targets-the-shaving-gel-and-foam-market/ (accessed 3.17.19).

Deshpande, N.S., Barigou, M., 2001a. Flow of gas-liquid foams through pipe fittings. Int. J. Heat Fluid Flow 22, 94–101. https://doi.org/10.1016/S0142-727X(00)00075-8

Deshpande, N.S., Barigou, M., 2001b. Foam flow phenomena in sudden expansions and contractions. Int. J. Multiph. Flow 27, 1463–1477. https://doi.org/10.1016/S0301-9322(01)00017-9

Deshpande, N.S., Barigou, M., 2000. The flow of gas-liquid foams in vertical pipes. Chem. Eng. Sci. 55, 4297–4309. https://doi.org/10.1016/S0009-2509(00)00057-9

Dollet, B., 2010. Local description of the two-dimensional flow of foam through a contraction. J. Rheol. (N. Y. N. Y). 54, 741–760. https://doi.org/10.1122/1.3380852

Dollet, B., Elias, F., Quilliet, C., Raufaste, C., Aubouy, M., Graner, F., 2005. Two-dimensional flow of foam around an obstacle: Force measurements. Phys. Rev. E - Stat. Nonlinear, Soft Matter Phys. 71, 1–11. https://doi.org/10.1103/PhysRevE.71.031403

Dollet, B., Graner, F., 2007. Two-dimensional flow of foam around a circular obstacle: Local measurements of elasticity, plasticity and flow. J. Fluid Mech. 585, 181–211. https://doi.org/10.1017/S0022112007006830

Durian, D.J., 1997. Bubble-scale model of foam mechanics:mMelting, nonlinear behavior, and avalanches. Phys. Rev. E 55, 1739–1751. https://doi.org/10.1103/PhysRevE.55.1739

Eliceiri, K., Schneider, C.A., Rasband, W.S., Eliceiri, K.W., 2012. NIH Image to ImageJ : 25 years of image analysis. Nat. Methods 9, 671–675. https://doi.org/10.1038/nmeth.2089

Ferreira, T., Rasband, W., 2012. ImageJ User Guide User Guide IJ 1.46, 1–198.

Graner, F., Dollet, B., Raufaste, C., Marmottant, P., 2008. Discrete rearranging disordered patterns, part I: Robust statistical tools in two or three dimensions. Eur. Phys. J. E 25, 349–369. https://doi.org/10.1140/epje/i2007-10298-8

Jabarkhyl, S., Barigou, M., Badve, M., Zhu, S., 2020. Rheological properties of wet foams generated from viscous pseudoplastic fluids. Innov. Food Sci. Emerg. Technol. 102304. https://doi.org/10.1016/j.ifset.2020.102304

Jay, P., Magnin, A., Piau, J.M., 2002. Numerical Simulation of Viscoplastic Fluid Flows Through an Axisymmetric Contraction. J. Fluids Eng. 124, 700. https://doi.org/10.1115/1.1486472

Jones, S.A., Cox, S.J., 2012. On the effectiveness of a quasistatic bubble-scale simulation in predicting the constriction flow of a two-dimensional foam. J. Rheol. (N. Y. N. Y). 56,

457–471. https://doi.org/10.1122/1.3687301

Jones, S.A., Dollet, B., Slosse, N., Jiang, Y., Cox, S.J., Graner, F., 2011. Two-dimensional constriction flows of foams. Colloids Surfaces A Physicochem. Eng. Asp. 382, 18–23. https://doi.org/10.1016/j.colsurfa.2010.11.054

Langlois, V.J., 2014. The two-dimensional flow of a foam through a constriction: Insights from the bubble model. J. Rheol. (N. Y. N. Y). 58, 799–818. https://doi.org/10.1122/1.4872058

Lim, K.S., 2005. Studies of foam microstructure and rheology. PhD Thesis. University of Birmingham. United Kingdom.

Marmottant, P., Raufaste, C., Graner, F., 2008. Discrete rearranging disordered patterns, part II: 2D plasticity, elasticity and flow of a foam. Eur. Phys. J. E 25, 371–384. https://doi.org/10.1140/epje/i2007-10300-7

RAM, 2018. Global Polyurethane Foams Market Size, Market Share, Application Analysis, Regional Outlook, Growth Trends, Key Players, Competitive Strategies and Forecasts, 2018 To 2026 [WWW Document]. URL https://www.researchandmarkets.com/reports/4620334/global-polyurethane-foams-market-size-market (accessed 3.15.19).

RAM, 2013. Global Retail Ice Cream Industry 2013-2018: Trends, Profits and Forecast Analysis [WWW Document]. URL https://www.researchandmarkets.com/research/2n6zfd/global_retail_ice (accessed 3.15.19).

Thielicke, W., Stamhuis, E.J., 2014. PIVlab – Towards User-friendly, Affordable and Accurate Digital Particle Image Velocimetry in MATLAB. J. Open Res. Softw. 2. https://doi.org/10.5334/jors.bl

Wiggers, F.N., Deshpande, N.S., Barigou, M., 2000. The Flow of Foam Films in Vertical Tubes. Chem. Eng. Res. Des. 78, 773–778. https://doi.org/10.1205/026387600527789